Processing Strategies to Obtain Highly Porous Silk Fibroin Structures with Tailored Microstructure and Molecular Characteristics and Their Applicability in Water Remediation

A. Reizabal[1,2*], C.M. Costa[3,4], P. G. Saiz[1], B. Gonzalez[5], L. Pérez-Álvarez[1,2], R. Fernández de Luis[1], A. Garcia[5], J.L. Vilas-Vilela[1,2], S. Lanceros-Méndez[1,6,]

[1]BCMaterials, Basque Center for Materials, Applications and Nanostructures, UPV/EHU Science Park, 48940 Leioa, Spain

[2]Departamento de Química Física, Facultad de Ciencia y Tecnología, Universidad del País Vasco/EHU, Apdo. 644, Bilbao, Spain

[3]Centro de Física, Universidade do Minho, 4710-057 Braga, Portugal

[4]Centro de Química, Universidade do Minho, 4710-057 Braga, Portugal

[5]Advanced Mining Technology Center (AMTC), Universidad de Chile, Av. Tupper 2007, Santiago 8370451, Chile

[6]Ikerbasque, Basque Foundation for Science, 48013 Bilbao, Spain

Abstract: The present work reports on the control of silk fibroin (SF) porous structures performance through various processing methods. The study includes the analysis of two dissolving techniques ($CaCl_2/H_2O$/EtOH ternary and $LiBr/H_2O$ binary solutions), three regeneration methods (gelation, lyophilization and gas foaming) and one post-processing (EtOH). In all the cases, followed steps lead to SF structures with porosity values above 94% and large surface areas. Also, results about samples microstructure, secondary organization, crystallinity and water behavior, reveal a direct correlation between processing and SF properties.

Thanks to the achieved progress, the SF varying porous structures were evaluated for metalloids (As^{5+} and As^{3+}) and heavy metals (Cr^{6+} and Cr^{3+}) adsorption, observing a direct relationship between samples processing and ionic species adsorption ability.

Thus, it is shown that the control of the properties of SF based porous structures through processing, represents a suitable and ecofriendly approach for the development of bio-based materials for environmental applications.

Keywords: Silk fibroin; porous microstructure; adsorption mechanism, heavy metals removal; water remediation.

1. Introduction

Sustainability is a global priority implying the proper use of global resources and the reduction of non-renewable materials dependence [1, 2]. In particular, oil-based materials lead to a large environmental impact related to extraction procedures, combustion and waste management [3]. Thus, it becomes essential to redirect efforts towards the development of a new generation of materials able to respond to the technological demands, by matching the advantages of synthetic materials, but supporting the decreasing of current pollution levels [4].

In this scope, bio-based materials obtained from natural resources, appear as an interesting alternative. Among them, Silk Fibroin (SF) a polypeptide fiber found in the cocoons of Bombyx mori silkworms, and used in fabrics for more than 3000 years [5, 6], represents an interesting option, due to its natural origin, availability and physical and chemical properties [7]. SF shows excellent thermal and chemical stability, high mechanical strength, biodegradability and facile processing [14]. Also, it is possible to enlarge SF applicability by varying its structure in the form of fibers [8], films [9], particles [8], non-woven mats [10] and tri-dimensional (3D) porous structures, among others [11]. Thanks to that, it has been possible to apply SF in electronics [12, 13], sensors and actuators [9, 14], biomedicine [15] and environmental remediation [16-18]. Specially, SF has become a promising material in the environmental field, where it has been used as filtration and decontamination media [16, 19]. However, there is still a lack of knowledge around how processing procedure affects SF based materials microstructure and properties, which is particularly relevant for the improvement of SF for specific applications [20].

As a protein, SF consists on repetitive amino acid sequences mainly composed by two polypeptide chains with different molecular weight, a 390-kDa heavy chain (H-Chain) and 26-kDa light chain (L-Chain) [5, 6], bonded together by a single disulfide bond [15]. H-chains are related with repetitive G(Glycine)-A(alanine)-G-A-G-X hydrophobic motifs (crystalline domains), while L-chains are related to non-repetitive hydrophilic ones (amorphous region) [16]. This amphiphilic organization based on hydrophilic–hydrophobic–hydrophilic blocks confers SF a similar behavior to that observed for triblock-copolymers in solution [21].

During secondary folding, SF polypeptide chains adopt different conformations, which strongly influence the final behavior of SF. These configurations are i) random coil (RC), composed by non-ordered domains; ii) α-helix (A), a ordered region based on a tight

single polypeptide chain with helix conformation; iii) β-sheets (B), which are two dimensional sheet-like ordered regions of folded polypeptide chains linked by hydrogen-bonds (Figure 1b); iv) β-turns (T), a non-ordered domains implied on β-sheets linking and v) side chains (SC), which are peptide residues non-implied in bonding.

There are three known crystalline conformations of SF named Silk I, Silk II and Silk III [22]. Silk I can be defined as the precursor structure of β-crystals, is formed by a mainly ordered structure (composed by G-A-G-A-G- repetitive motif) in where the complete packing is hindered by interactions between water molecules and ordered domains. As a consequence, Silk I show a metastable conformation easy to be solubilized. Silk II is a highly packed structure and results from Silk I stabilization after the bonded-water molecules lost. Ordered domains packing into silk II leads to the formation of non-soluble β-sheets, which give to the structure stability [23]. Silk III is an uncommon threefold helical crystal structure formed at the air-water interface [24].

During SF regeneration, β-crystals from several polypeptide chains packing are formed. As a result, SF structure adopts a cross-linked conformation where β-crystals act as nodes linking the amorphous regions. The high stability of β-crystal nodes enables the overall structure integrity, while wrinkled amorphous domains provide mobility, elasticity and flexibility to the SF structure [25, 26]. The SF characteristics are defined by the convergence of multiple factors, such as the presence and ratio between crystalline and amorphous domains, their relation into the cross-slinked structure, as well as the crystalline domains organization and non-folded chains amphiphilic behavior. Accordingly, the controlled modification of the abovementioned characteristics represents an interesting tool in order to endow SF based materials of specific applicability. Thus, in this work their study and control have been prioritized.

Based on this idea, the present work focuses on establishing the effect of different processing strategies to tailor SF microstructure and properties. For that, two dissolving techniques ($CaCl_2/H_2O$/EtOH ternary and $LiBr/H_2O$ binary solutions), three different processing methods (gelification, lyophilization and gas foaming)[27-30] and one post-processing (EtOH treatment), have been used to produce SF based porous structures and tailor their properties. The above described SF processing approaches correspond to a green strategy where water-based solvents with low environmental impact have been used. It is worthy to note that the developed techniques are characterized by low complexity and high availability [31], **a** strategy that could facilitate their implementation and replication in future investigations. In parallel, the selected processing methods

allowed controlling the SF molecular recombination time (i.e. gelation > lyophilization > gas foaming) before their freeze-drying, while the use of EtOH as β-sheets promoter [32], allows even a further control of the SF final structure and properties.

In order to prove the relevance of shaping the porous and molecular structures of SF towards its application on water pollution remediation, the processed biomaterials have been tested over the adsorption of highly hazardous arsenic and chromium model pollutants. Heavy metal water pollution is a serious environmental issue, since many places worldwide show a natural concentration of these inorganic ions above the legal limits. Indeed, arsenic and chromium exhibit acute toxicity in aqueous environments (e.g. genotoxic, mutagenic, teratogenic and carcinogenic), are non-biodegradable and long-term persistent, even when present at very low concentrations [2, 33]. In addition, their varied chemistry and speciation, as well as their high solubility and mobility, makes current technologies inefficient to lower their concentration below the legal limits.

In this regard, one of the most promising technologies to achieve an efficient water pollutant removal are composite materials [34], which are based on an active phase on which the pollutant is adsorbed and a non-active structure providing support and mechanical stability. Thus, commonly, the adsorption capacity of a composite system is mainly defined by the adsorption capacity of active phase and the accessibility given by the holding phase, the latter mainly depending on its porosity [35]. Whereas most efforts in this area have been devoted to improving the efficiency of the active phase, few investigations have been directed to improve the self-adsorption properties of the porous polymer structures. In this context and promoted by the control achieved on SF porous and molecular structures, a proof of concept study centered on bio-based materials applied for adsorption purposes has been carried out. It is to notice that the obtained materials can be further complemented with an active/selective phase in order further improve its characteristics for polluted waters remediation. The main hypothesis of our work is that the adsorption capabilities of SF over metal ions can be tuned just modifying porous and molecular structure through simple and accessible techniques. This approach does not exclude the possibility to complement the capabilities of the SF materials with other active phases that can endow them of additional pollutant adsorption capacity and affinity. It is worthy to mention too, that some metal industrial processes, such as chromium plating industry, led to metal, and specifically to Zn, Cd, or Cr high concentrated solutions, with ppm values even higher that the ones studied in this work [36]. Therefore, the relevance of the SF materials could go beyond solely the water de-pollution purposes.

Indeed, their application in industrial output waters could be another interesting application of the developed bio-materials.

2. Experimental details

2.1. Materials

Silk Fibroin (SF) was extracted from *Bombyx mori* cocoons, supplied by APPACDM from Castelo Branco (Portugal). Sodium carbonate (Na_2CO_3), calcium chloride ($CaCl_2$) and lithium bromide were purchased from Sigma-Aldrich. Dialysis tubes with a diameter of 3 cm and molecular weight cut-of 3500 Daltons were obtained from Spectrum.

2.2. *Precursor solution preparation*

Porous structures were prepared from aqueous solutions of SF. The first step was the extraction of SF from the *Bombyx mor*i Silk cocoons. For this, the cocoons were dry-cleaned and cut into small pieces of about 0.5 cm^2. The pieces were then degummed twice in 3.7 mM Na_2CO_3 aqueous solutions at 80-85 ^oC during 10 minutes in a silk-to-liquid ratio of 1:40 (wt:v). Between first and second degumming the fibers where manually opened to facilitate the process. The resulting SF was immersed three times in consecutive distilled water baths and then rinsed thoroughly. The well-cleaned fibers were finally dried in an oven at 40 ^oC for 24 h and then kept in dry until be used.

Afterwards, SF was dissolved by following two different procedure, as a result, two types of aqueous SF solutions will be obtained. The main difference between both procedures was the used solving agent: i) a $CaCl_2/H_2O$/EtOH ternary solution 1/8/2 molar in a silk-to-liquid ratio of 1:10 wt:v and ii) 9.3 M $LiBr/H_2O$ binary solution in a silk-to-liquid ratio of 1:20 wt:v. In both cases, SF was dissolved for 2 h at 60 ^oC under magnetic stirring. The obtained solutions were dialyzed against distilled water in a 3500 Da cutoff cellulose cassette, with 3 water changes per day and until constant dialyzed water conductivity was achieved. The resultant SF aqueous solution with a concentration around 0.1 g/ml was used directly for the next steps. The SF aqueous solutions concentration was measured by drying a controlled solution volume and weighing the residues.

2.3. Porous structures processing

As schematically represented in Figure 1, SF porous structures were prepared by lyophilisation, but aqueous solutions were differently treated before this final step.

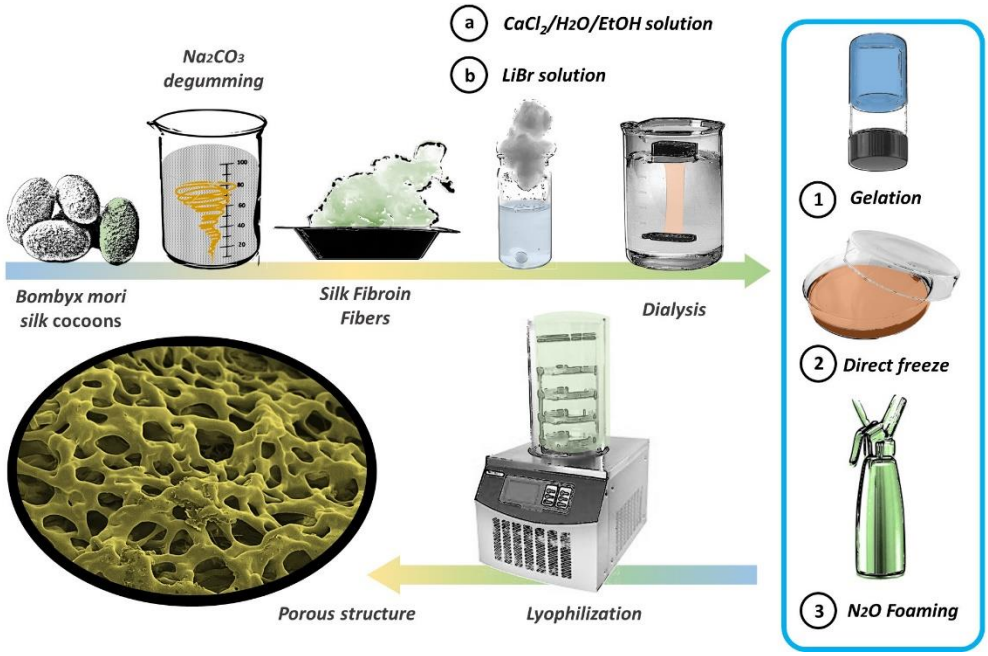

Figure 1 – Schematic representation of the preparation procedures of the SF structures.

The methods involve: i) the gelation of aqueous solution, placing it statically at 25 ºC for 24 hours; ii) the use of the aqueous solution directly and iii) foaming aqueous solution by using a whip siphon, nitrous oxide (N_2O) as pressure gas and a nozzle of 6 cm long and 1 cm diameter. Gelled and direct samples were frozen at -20 ºC during 12h, while foam samples were fast freeze by liquid nitrogen. Table 1 shows the identification data of the samples, indicating also the dissolving agent, the processing method and the time elapsed since the samples are prepared until they completely freeze.

In order to induce the secondary structures conversion to highly stable β-crystals, all of SF structures were treated with EtOH [32]. For this, samples were immersed for 5 seconds in EtOH and dried for 12 h at room temperature. Samples treated with EtOH will be identified with the EtOH code at the end of the names presented in Table 1.

Table 1 - SF porous structures identification and main processing parameters

Sample	*Dissolving Agent*	*Processing*	*Time (h)*

CaCl-Gel	$CaCl_2/H_2O/EtOH$	gelation + freezing (-20ºC) lyophilisation	27-28
CaCl-Lio	$CaCl_2H_2O/EtOH$	freezing (-20ºC) + lyophilisation	3-4
CaCl-Foam	$CaCl_2/H_2O/EtOH$	NO_3 foaming + N_2 freezing + lyophilisation	0
LiBr-Gel	$LiBr/H_2O$	gelation + freezing (-20ºC) lyophilisation	27-28
LiBr-Lio	$LiBr/H_2O$	freezing (-20ºC) + lyophilisation	3-4
LiBr-Foam	$LiBr/H_2O$	NO_3 foaming + N_2 freezing + lyophilisation	0
CaCl-Gel-EtOH	$CaCl_2/H_2O/EtOH$	gelation + freezing (-20ºC) lyophilisation + EtOH	27-28
CaCl-Lio-EtOH	$CaCl_2H_2O/EtOH$	freezing (-20ºC) + lyophilisation + EtOH	3-4
CaCl-Foam-EtOH	$CaCl_2/H_2O/EtOH$	NO_3 foaming + N_2 freezing + lyophilisation + EtOH	0
LiBr-Gel-EtOH	$LiBr/H_2O$	gelation + freezing (-20ºC) lyophilisation + EtOH	27-28
LiBr-Lio-EtOH	$LiBr/H_2O$	freezing (-20ºC) + lyophilisation + EtOH	3-4
LiBr-Foam-EtOH	$LiBr/H_2O$	NO_3 foaming + N_2 freezing + lyophilisation + EtOH	0

2.4. *Characterization techniques*

The morphology of the structures was evaluated by scanning electron microscopy (SEM) with a NanoSEM - FEI Nova 200 (FEG/SEM). Prior evaluation, all the samples were coated by a 20 nm gold layer by magnetron sputtering with a Polaron SC502 apparatus. The SF materials have been fully characterized by mercury porosimetry, FTIR, XRD and DSC. Experimental details are provided in as supplementary information.

Both water uptake and water stability were measured by the same experiment. For that, the weight of SF porous structures immersed in water was measured during consecutive 5 days. Water uptake (U %) was obtained from the relation between absorbed water and initial mass, following the equation 1.

$$U\ (\%) = \frac{M_s - M_d}{M_d} \times 100 \quad (1)$$

where U is the samples water uptake ability (%), M_s is the weight of the swollen sample in equilibrium (g) and M_d is the weight of dried sample (g). The total water uptake was obtained once samples stop absorbing water and show constant mass.

Water stability was measured by following the weight measurements over time, with the maximum water load as reference. Samples degradation was considered when weight loss is observed, while constant weight measurement signaled samples water stability.

2.5. Adsorption test

In order to carry out the pollutants adsorption experiments, 20 ppm solutions of metalloids (As^{5+}, As^{3+}) and heavy metals (Cr^{6+} and Cr^{3+}) were prepared, from the following precursor salts: As^{5+} - Na_2HAsO_4 (≥ 98 %), As^{3+} - $NaAsO_2$ (90 %), Cr^{6+} - $K_2Cr_2O_7$ (99.8 %) and Cr^{3+} - $KCrSO_4$•$12H_2$. The solutions pH was adjusted to 4 by adding HCl and NaOH diluted solution. For all the experiments the sample/solution ratio was fixed to 2 g/L. Thus, 10 mg of silk were added to 5 mL of solution, and mechanically stirred at room temperature for 18 hours. Afterwards, silk structures were manually separated from the solution, and the final concentrations of chromium and arsenic were determined by slightly modified diphenylcarbazide [37, 38] and heptamolybdate [39, 40] colorimetric methodologies, respectively. Absorbance of the solutions was measured by a Spectronic 20 Genesys UV-Vis spectrophotometer. Triplicate punctual adsorption measurements were performed for all the samples.

3. Results

3.1. Morphological characterization

SEM images were used to analyse the morphology and pore microstructure of the developed SF structures. Representative images of the six different samples, CaCl-Gel, CaCl-Lio, CaCl-Foam, LiBr-Gel, LiBr-Lio and LiBr-Foam, are presented in Figure 2. Further information related to morphology is shown as supporting information (Figure S1). As can be observed, all the samples are characterized by a well-defined porous structure. In addition, the shape of the pores within the structures clearly differs from one another sample, demonstrating the strong effect of the solving agent and the regeneration procedure on the final morphology and structure of SF.

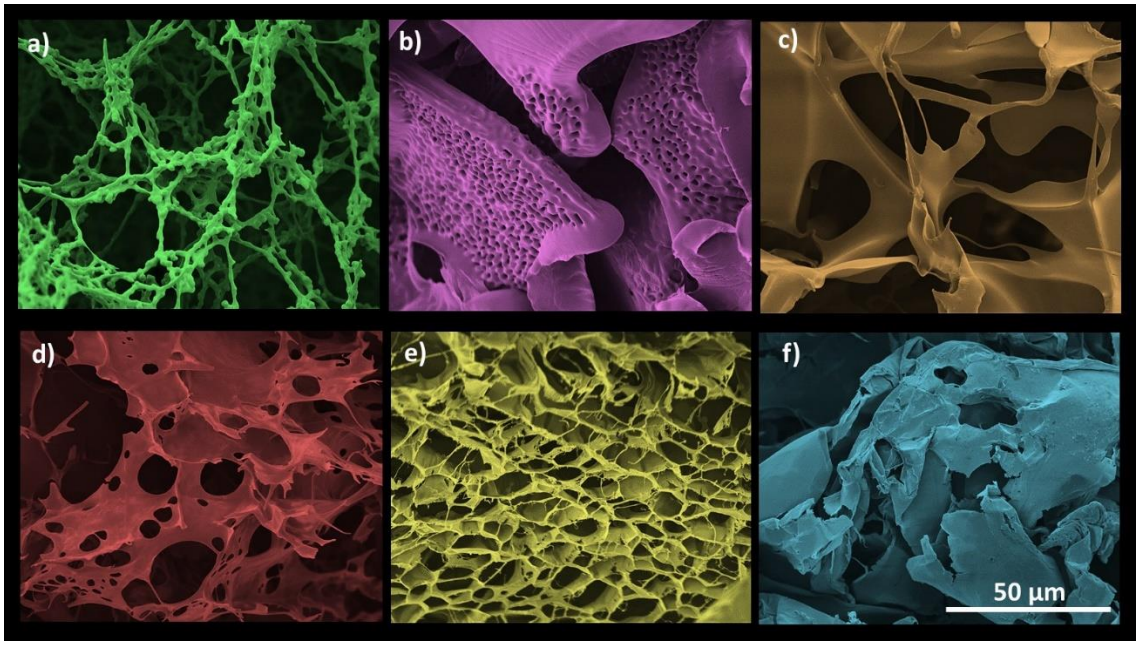

Figure 2 – Representative SEM images of the SF porous structures: a) $CaCl_2$-Gel b) $CaCl_2$-Lio c) $CaCl_2$-Foam d) LiBr-Gel e) LiBr-Lio and f) LiBr-Foam. g) LiBr-Lio sample after EtOH treatment. The scale is valid for all images. The colours were added digitally.

Figure 2a shows the morphology of $CaCl_2$-Gel sample, which is dominated by a highly branched network of fibrils. Each SF-based fibril is formed by elongated structures of 1-2 µm in thickness connected to globular structures of 2-3 µm of diameter. The set forms

a bean-like structure with interconnected and continuous pores ranging from 20 μm to 40 μm of diameter.

Both Gel samples were equally processed but with varying the solvent. This change leads to the formation of a completely different microstructure (Figure 2d). LiBr-Gels are composed by two-dimensional non-compact sheets, packed in a leaf-like macrostructure (Figure S1d) with an interconnected continuous pore system. The planar sheets of LiBr-Gel are characterized by a thickness between 200 - 400 nm with interspersed pores in the 2 μm to 20 μm diameter range, leading to a pore system with two pores levels.

Figures 2b and 2e show the morphology of $CaCl_2$-Lio and LiBr-Lio samples, respectively, both characterized by a leaf-like macrostructure (Figures S1b and S1e, respectively), but different microstructure. The morphology of the $CaCl_2$-Lio sample is formed by wide two-dimensional planar structures of 7-8 μm thickness, interspersed by small and homogeneously distributed pores of 1-2 μm diameter (Figure 2b). LiBr-Lio sample on the contrary, is composed by narrow planar structures with a thickness of 1-3 μm that fold in specific locations to form a sponge like/ honeycomb regions with irregular pores of 4-15 μm diameter (Figure 2e). In both cases, the existence of two-porosity levels leads to an overall porous structure with highly interconnected cavities.

Regarding the structures obtained by the N_2O foaming method, the morphology of the $CaCl_2$-Foam and LiBr-Foam samples (Figures 2c and 2f, respectively) also shows a leaf-like shape macrostructure. The main difference between the two samples is found in the thickness of the flat sheets, varying between 2 μm and 7 μm for $CaCl_2$-Foam and between 300-600 nm for the LiBr-Foam. Contrary to Gel and Lio samples, Foam samples do not show interspersed pores.

The effect of EtOH treatment on the porous SF structures can be observed in Figure 2g for the LiBr-Lio structure, being representative for the rest of the structures. After the treatment with EtOH, samples retain their porous structure, but with slight variations in the planar sheets conformation and a certain increase of the pore size.

Further insights on the structural characteristics of the samples were studied after mercury intrusion porosimetry, allowing to obtaining density, surface area and total porosity, as presented in Table 2.

Table 2 - Degree of porosity, density and surface area of the different SF-based structures ("-" indicates the lack of measurable data).

Sample	*Micropore size (μm)*	*Total porosity (%)*	*He density (g/cm^3)*	*Surface area (m^2/g)*	*Specific surface area (10^7 m^2/m^3)*
$CaCl_2$-Gel	20-40	94.0	1.34	71.1	4.47
$CaCl_2$-Lio	1-2	97.8	1.31	108.8	8.31
$CaCl_2$-Foam	-	94.9	1.42	45.5	3.20
LiBr-Gel	2-20	94.3	1.46	86.1	5.90
LiBr-Lio	4-15	93.7	1.64	59.6	3.63
LiBr-Foam	-	95.9	1.44	122.8	8.53

Regardless of the preparation procedure, the degree of porosity varies between 94% and 98%, which is significantly higher than the reported porosity values of comparable porous structures based on SF, which generally range between 70% and 90% [11, 16].

The specific surface areas range from 3.2×10^7 m^2/m^3 to 8.53×10^7 m^2/m^3, which are also higher than the values obtained for SF non-woven mats, commonly used for the preparation of membranes for environmental remediation [16, 17].

Mercury (Hg) intrusion curves as a function of pore diameter for the different structures were collected in Supporting Figure 2, showing that the intrusion values range between 1 and 300 μm, that indicates that all SF samples can be classified as macro-porous.

The main contributions to the final porosity differ between the different samples (Supporting Information, Figure S2). $CaCl_2$-Gel and LiBr-Gel samples show a pore distribution mainly centered at 13 μm pore diameter. But, $CaCl_2$-Gel shows intrusion signals at 30 μm, while LiBr-Gel shows them in the region above 1 μm. These data suggest that even when the two gel samples are highly dominated by 13 μm diameter pores, there are also relevant contributions of larger pores in the case of $CaCl_2$-Gel and smaller pores in LiBr-Gel, in good agreement with the microstructure observed at the corresponding SEM images (Figure 2).

$CaCl_2$-Lio and LiBr-Lio samples show peaks with a maximum at 54 μm, being also contributions of even larger pores (around 200 μm) in both cases. Thus, the Lio process leads to average larger pore sizes. The slight signal in the region of smaller pore diameters on $CaCl_2$-Lio sample can be related to the secondary pores observed in the SEM images (Figure 2b).

Finally, the intrusion results from $CaCl_2$-Foam and LiBr-Foam samples show a wide and oscillatory signal ranging between 0.8 to 200 μm. This porosity distribution indicates that, in contrast to Gel and Lio samples, with pores size defined at 13 and 200 μm, respectively, the pores of Foam samples are not in a well-defined diameter range.

3.2. Molecular and structural conformations

FTIR measurements were performed to evaluate the molecular conformations of SF in the different samples (Figure 3). As can be observed in Figure 3a, regardless of the solvent agent and processing method, the main absorption bands characteristic of SF, amide I - 1620 cm^{-1}, amide II - 1517 cm^{-1} and amide III - 1235 cm^{-1} remain unaltered. Comparing the FTIR spectra, the unique difference relies on the appearance of new absorption bands located at 2850 cm^{-1} (marked by black arrow), found for $CaCl_2$-Gel and LiBr-Gel samples.

Figure 3b shows the deconvolution of the FTIR spectra in the amide I region, providing information on the secondary organization of SF [41]. The possible secondary conformations are α-helix (A), β-sheets (B) and β-turns (T) belonging to crystalline domains and random coils (RC), and non-bonded side chains (SC), belonging to amorphous region. Each one, can be classified inside Amide I region according to its maximum wavenumber, in the following way: T (1696-1663 cm^{-1}), A (1662-1656 cm^{-1}), RC (1655-1638 cm^{-1}), B (1637-1616 cm^{-1} and 1705-1695 cm^{-1}) and SC (1615-1605 cm^{-1}) [42]. The presence of each conformation was estimated by the area under the IR curve for all the peaks corresponding to the same conformation.

Figure 3b shows two examples of the FTIR amide I deconvolution. In the upper part, a typical example of amorphous SF is presented where the maximum is located in the RC region. The lower part of Figure 3 shows an example of a highly crystalline SF structure, with maximum value in the B region, corresponding to β-sheet conformation.

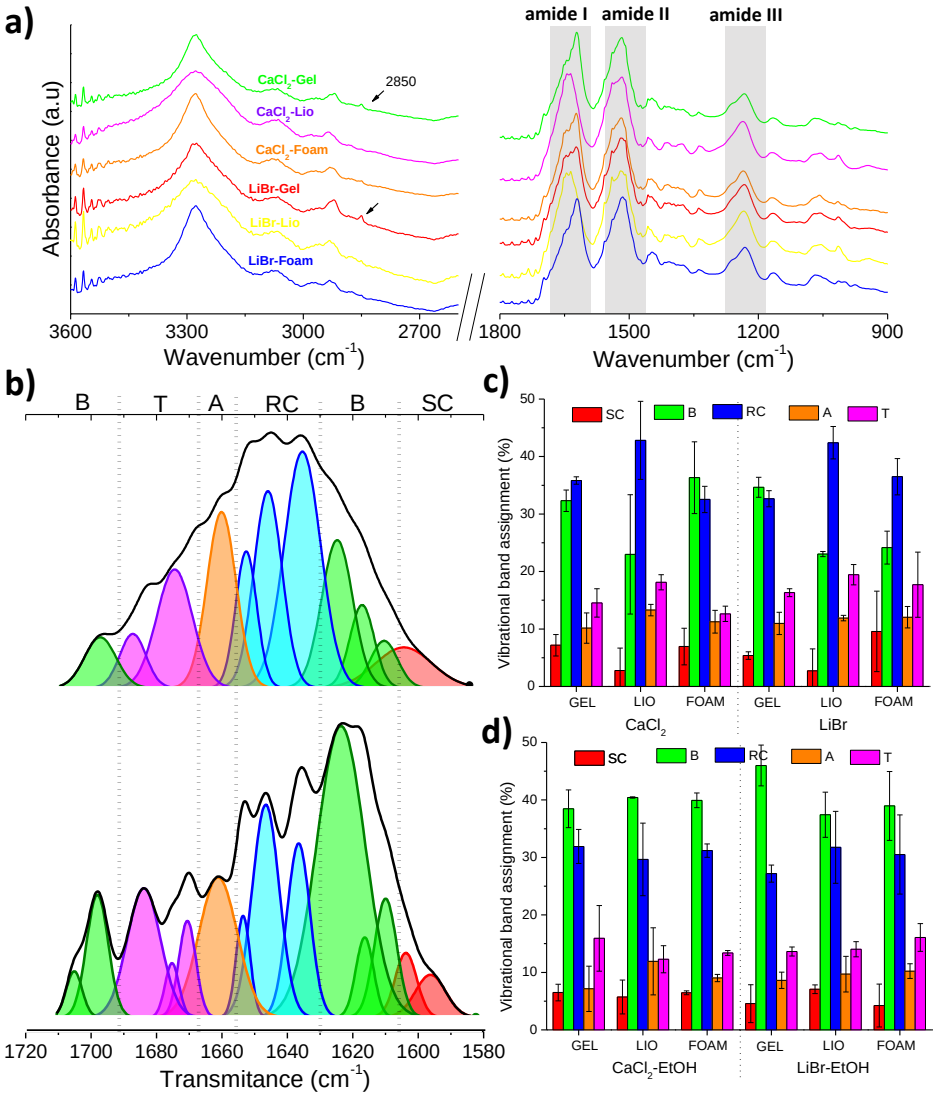

Figure 3 – For the different SF structures: a) FTIR absorbance curves, b) amide I deconvolution of the amorphous structure (above) and crystalline structure (below), c) band assignment and d) band assignment of SF-EtOH treated samples.

Figures 3c shows the secondary conformation of SF structures. Differences are observed among them, showing the influence of the processing conditions on the SF secondary structure and therefore, on the final properties of materials. In order to analyze those differences, statistical analysis of variance (ANOVA) under 5% of tolerance has been applied. Due to their influence on SF properties, β-sheets (B) content and the relation between B and random coil (RC) structures have been considered as the most important parameters to analyze by this method. Regarding to the ability of the different processing methods to promote the presence of β-sheets into SF structure, it is only observed a significant difference ($p < 0.05$) in Gelled samples, where followed processing seems to

have major ability to induce B structures (between 32 and 34%). Regarding to the relation between B and RC, it is observed a significant difference in lyophilized samples, which are clearly dominated by RC (~ 45%). In any case, no significant difference ($p>0.05$) between solving agents was observed.

The effect of EtOH treatment over SF porous structures is presented in Figure 3d. Following with ANOVA statistical analysis, it can be observed that there exists a significant increase of B structures (reaching to values around 40-45%.), when SF samples are treated with EtOH. The achieved similar values for β-structures in all the samples suggest the homogenous effect of EtOH over SF.

To analyze crystalline structures condition, X-ray data was used. It is important to consider that SF is formed by macromolecular chains, and therefore, it is unable to adopt a perfect crystalline structure with well-defined order. In contrast, SF crystallization is associated with the partial alignment of the molecular chains. This pseudo-packing leads to low crystalline diffraction patterns, accompanied by superimposed broad peaks ascribed to the not ordered regions. Further, the plasticization level of crystalline structures, represents a certain variability of crystalline spacing and consequently it is common to observe a slight displacement of diffraction peaks among samples [43, 44]. Figure 4 shows the X-ray diffraction patterns of the different samples. SF porous structures seem to reveal five different diffraction maxima at 12.4º, 14.5º, 20.1º, 24.9 º and 28.5º, which do not necessarily appear in all samples. Peaks 12º-13º, 14º-15º and >28º are commonly related with silk I structures [45], while the presence of peaks at 20-21º and 24-25 º is ascribed to highly packed silk II conformations [45, 46]. The apparent lack of silk III representative maxima suggests that the used processing methods do not promote these structures, mainly ascribed to water-air interfaces.

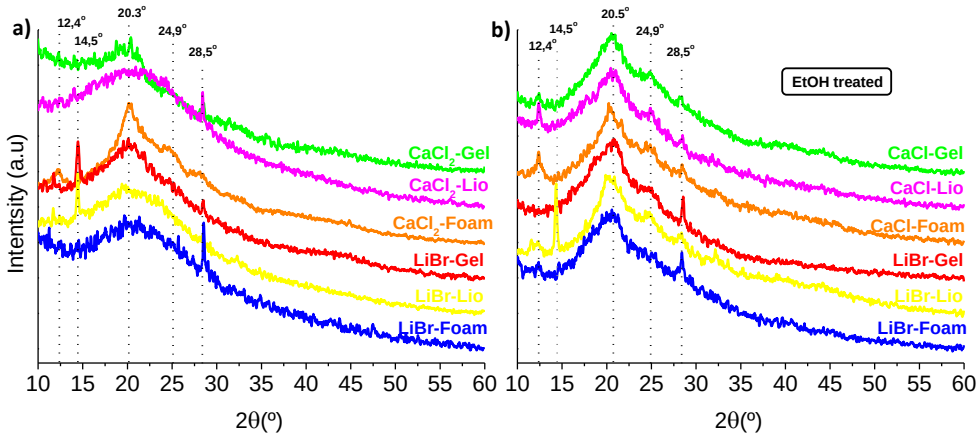

Figure 4 - X-ray diffraction patterns of a) SF porous samples and b) EtOH treated SF porous samples.

X-ray data suggest that i) processing methodology induces different ordering on crystalline structures, ii) Lio samples show the higher disorder degree, as revealed the broader diffraction peaks and iii) LiBr samples exhibit more non-stabilized Silk I structures, as revealed by the well-defined diffraction maxima observed around 12.4, 14.5 and 28.5º in 2θ (Figure 4a).

From the crystallographic structural point of view, the EtOH post-treatment of the samples has two side effects. Firstly, it modifies the crystals patterns of all the samples situating their maximum at 20-21º in 2θ, ascribed to Silk II structure. Secondly the broad diffraction signals ascribed to amorphous disorder domains is reduced.

3.3. Thermal behaviour

The thermal behavior of the SF structures was studied by TGA and DSC (Figure 5). The TGA results (Figures 5a and 5b) show a similar weight loss profile as a function of temperature for all samples. Before 100 ºC, porous SF undergo a first weight loss due to water evaporation. Then, the weight of the samples remains constant until 290 ºC, temperature at which SF starts to degrade due to the side chains breakdown and peptide bonds cleavage [47, 48]. Finally, around 330 ºC the combustion of the organic compounds starts, and it is completed at around 600 ºC. The main difference between samples is found during water evaporation step (<100 ºC), in where $CaCl_2$ processed samples show a weight loss around 10% and LiBr samples around 5%.

The treatment with EtOH, on the contrary, promotes larger variations in the thermal degradation profiles (Figure 5a and 5b). On one side, EtOH treated samples show a minor weight decrease during the water loss step. On the other side, it can be observed that the following degradation steps shift to higher temperatures (from 290 ºC to 300 ºC), including complete combustion process, which ends at 615 ºC [49].

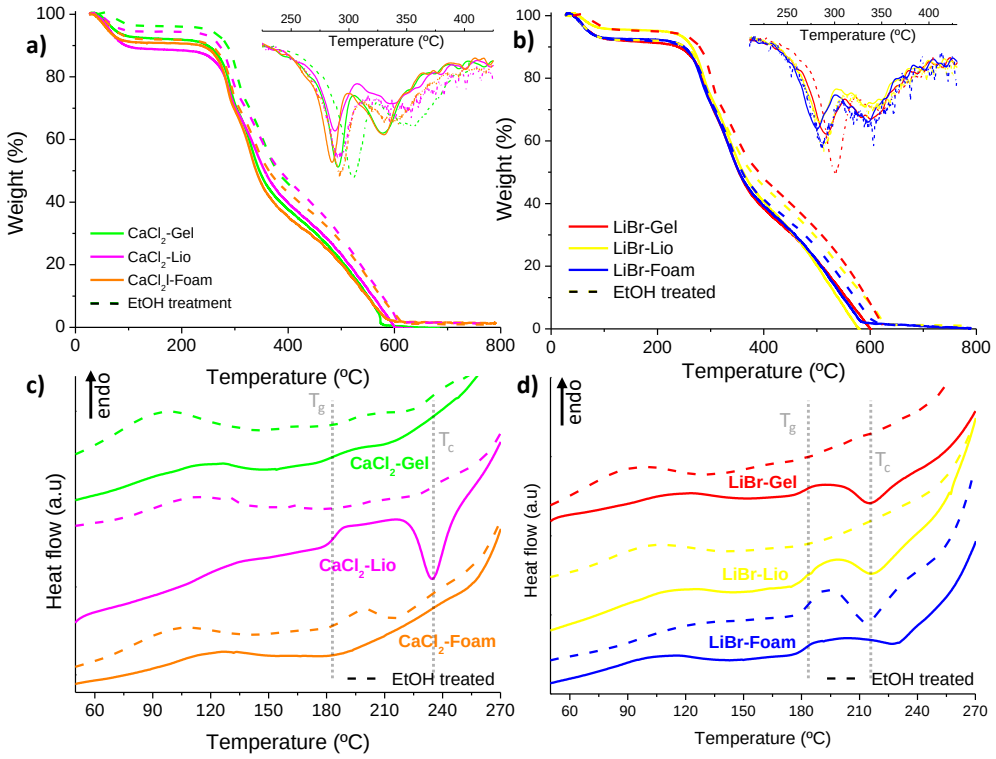

Figure 5 - TGA and DSC thermograms for $CaCl_2$-Gel, $CaCl_2$-Lio and $CaCl_2$-Foam samples (a and c) and LiBr-Gel, LiBr-Lio and LiBr-Foam samples (b and d), both pristine and treated with EtOH.

The thermal transitions of SF could be hidden by the endothermic peak related to the water evaporation. Thus, previous to the DSC measurements, water was removed from the samples by 20 min isothermal heating at 140 ºC. The DSC scans performed after that procedure are shown in Figure 5c and 5d. The main characteristic transitions of SF are a glass transition temperature (T_g) around 185 ºC , ascribed to amorphous domains motion [48], a recrystallization temperature (T_c) found as a exothermic peak between 210 - 235 ºC, attributed to the amorphous domains folding into β-sheet crystalline regions and the degradation peak above 250 ºC, related to the beginning of the side chains and peptide bonds thermal decomposition. The slight endothermic peak that can be observed in some samples before glass transition is related to the evaporation of remaining bounded water molecules [48].

As observed, Lio samples showed a well defined Tg and Tc, while the same transitions are slightly or non-visible in the other samples (Figure 5a and 5b).

After EtOH treatment, the thermal behavior becomes homogenous for all samples (dashed line in Figures 5c and 5d) and all thermal transitions of the porous structures disappeared which is directly related to the crystallization of amorphous domains (Figure 3).

3.4. Water uptake and stability

In order to apply SF-based porous materials for water pollution remediation purposes, it is highly desirable to fully understand samples behaviour in wet environments. Henceforth, water uptake and the water stability were measured.

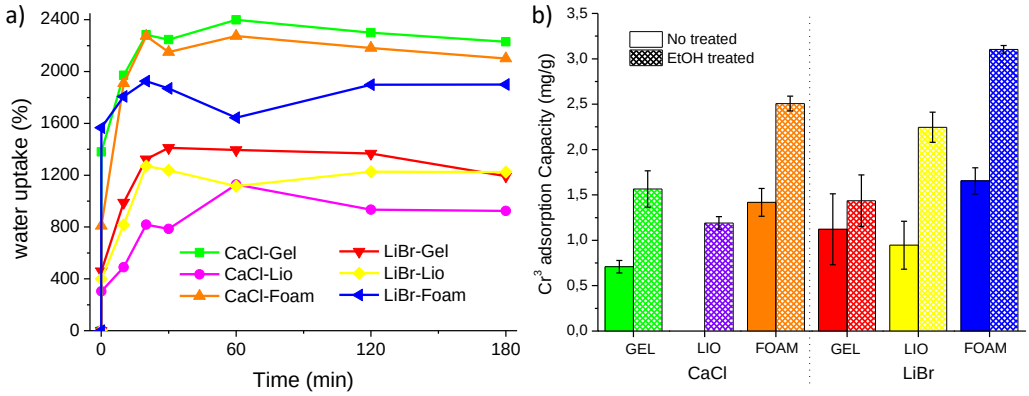

Figure 6- SF porous samples: a) water uptake, b) Cr^{3+} adsorption.

Water uptake was monitored during the first 180 min of immersion (Figure 6a). Samples water saturation point is shown in Supporting Figure 3a. As can be observed all the porous structures, reach a water uptake saturation after 20 minutes of immersion. Data point out the major adsorption of CaCl-Gel samples, with 24g/ml adsorption.

EtOH treated samples water uptake data is collected in Supporting Figures 3a and 3b. As can be observed, after EtOH treatment, water uptake appears to be reduced in all the cases, while water absorption speed and retention ability remains constant.

Water stability of SF structures was analysed by measuring the weight of the porous membranes after reached the maximum water uptake (Supporting Figure 3c). Data were collected for 3 consecutive weeks. After water immersion, practically all the samples show no significant weight loss, showing an excellent good stability. The $CaCl_2$-Lio sample was the only exception, resulting in a partial weight loss of nearly 50% of the total mass.

After treatment with EtOH, the porous structures conserve their water stability, even for the $CaCl_2$-Lio sample which becomes water stable. Results confirming the EtOH ability to stabilize SF structures (Supporting Figure 3d).

3.5. Heavy metals adsorption

The ability of the different porous SF structures to remove heavy metals from water was measured by water adsorption. SF samples were initially analysed versus different metalloids and heavy metal species: As^{3+}, As^{5+}, Cr^{6+} and Cr^{3+}. Supporting Figure 4, collects the LiBr-Foam sample adsorption capacities as representative for all the samples. The initial results indicate that significant pollutant reduction is attained just in the case of Cr^{3+}. To understand the effect of the morphology and the physical-chemical properties of porous SF structures in the Cr^{3+} adsorption ability, the adsorption capacity of each sample before and after EtOH treatment was analysed. The obtained adsorption results are represented in Figure 6b.

Figure 6b shows that all samples allow significant adsorption of Cr^{3+}, between 0.7 and 1.65 mg of Cr^{3+} per g of SF, indicating the suitable characteristics of the developed SF structures for water pollution remediation [50]. The maximum retention values, slightly below 20% of the total concentration, were observed for the samples processes as foams ($CaCl_2$-Foam and LiBr-Foam).

Further, the Cr^{3+} adsorption nearly doubles for all samples after the EtOH treatment, (1.2 and 3.1 mg/g). Once again, the maximum adsorption values are observed in the Foam samples, with adsorption capacities above 30% of the initial concentration.

4. Discussion

Silk fibroin porous structures have been processed following diverse procedures, including different solving agents, processing and post-processing. In the following, i) the origin of each morphology, ii) the effects of the processing and obtained microstructure on the physical-chemical properties of the material and iii) the potentials of the SF porous structures on water remediation will be discussed.

4.1. *SF porous structures formation*

During the solving, Ca^{2+} and Li^{+} cations from $CaCl_2$ and LiBr respectively, form chelates with SF carbonyl and hydroxyl groups, disrupting the intra- and intermolecular forces that keep the SF structure packed (Figure 7a1) [51]. Taking advance from the disruption, water molecules flow inside SF structure and form new H-bonds, leading to completely amorphous and opened SF conformation (Figure 7a2). In this point, SF molecules are free to interact with water generated polar environment [52] (Figure 7b1) and due to the SF amphiphilic behavior, the polypeptide chains adopt micelles-like structures, in where hydrophilic domains occupy the shell and hydrophobic blocks the core (Figure 7b2) [53]. As H. Cho *et al*. [54] described, during SF solution, strong ionic force of $CaCl_2$, promotes the polypeptide chains scission into smaller chains. As a consequence, when SF micelles are formed, the small polypeptide sections aggregate, leading to molecules with high hydrodynamic radius (ranging from 100 to 300 nm). On the contrary, this effect is not observable for LiBr solutions, in where SF molecules self-assemble to form micelles with smaller hydrodynamic radius (10 to 30nm) (Figure 7b2) [54]. During micelles folding, water molecules could get trapped inside, hindering the hydrophobic interactions and delaying structures complete packing.

When SF solution is freeze, due to SF/water solution eutectic point, the formed pure water ice crystals exclude the SF micelles, grouping them into ice crystal walls (Figure 7b3). The increasing SF concentration , favors the protein-protein interactions, giving place to a continuous phase formation, as observed in sheet-like structures of SEM images (Figure 2) [55]. The definitive porous structure is formed once ice crystals are removed by lyophilization, leaving the planar structures without further changes [55] (Figure 7b4).

As a result of the $CaCl_2$ micelles larger size, when they are accumulated into the ice crystals walls, thicker structures than those formed from LiBr smaller micelles are

promoted (Figure 7b4). This effect explains the difference on sheet-like structures thickness observed between samples processed by $CaCl_2$ and LiBr solutions (Figure 2). The nature of secondary order micro-pores, is related to the growth of secondary ice crystals embedded in highly concentrated SF regions [55]. Their size and shape respond to the dimensions of planar structures in where they are formed. The thicker structures formed in $CaCl_2$ samples represent a higher resistance to ice crystals growth than the narrower structures formed by LiBr processing. Thus, the formed secondary crystals from $CaCl_2$ ternary solution, adopt smaller and more regular shapes while secondary ice crystals of LiBr processed samples, with less resistance, facilitate the formation of bigger and more irregular pores. The lack of secondary pores on Foam planar structures, reveals that the faster freezing process of liquid nitrogen bath, does not provide enough time to form secondary ice crystals. The irregularity of foam samples pores sizes, could be related to N_2O gas molecules induced non-controlled cavities (Supporting Figure 2) [30].

The bean-like structure observed in CaCl-Gel samples is the one exception with respect to the microstructure (SEM images Figure 2 and Figure S1 in the supplementary information). Taking into consideration the given additional time for gelation (table 1), the observed bean-like structures must be related with molecular reorganization processes (Figure 7c). SF micelles have a tendency to group based on the formation of inter- and intramolecular interactions along the protein chains, including hydrophobic interactions and hydrogen bonds [28] (Figure 7c3). As described Z. Chen *et al.* [56] eventually, when SF micelles have enough time to interact one each other, they start growing in the form of elongated structures of repetitive micelles (Figure 7c4). These structures are named nano-fibrils and due to additional micelles junctions, nano-fibrils continue growing and branching until the formation of interconnected network (Figure 7c5) [56]. While fibrils remain still in solution, the water molecules trapped inside the micelles hinder the formation of crystalline structures [57]. However, when sufficient time for molecular interactions is given (as happened in Gel samples), the hydrophobic interactions finally happen, promoting the ordered domains packing into B ordered domains, which stabilize the structure and avoid its resolubilization [58] (Figure 7c6). During freeze, the formed fibrils will be slightly compacted by ice crystals grow (Figure 7c7), but due to the achieved stability, the network still remains unalterable (Figure 7c8). The larger micelles from $CaCl_2$ ternary solution seem to be the responsible of inducing more contacts between micelles, favoring larger hydrophobic interactions between them and supporting the fibrils network formation process in $CaCl_2$-Gel samples [58].

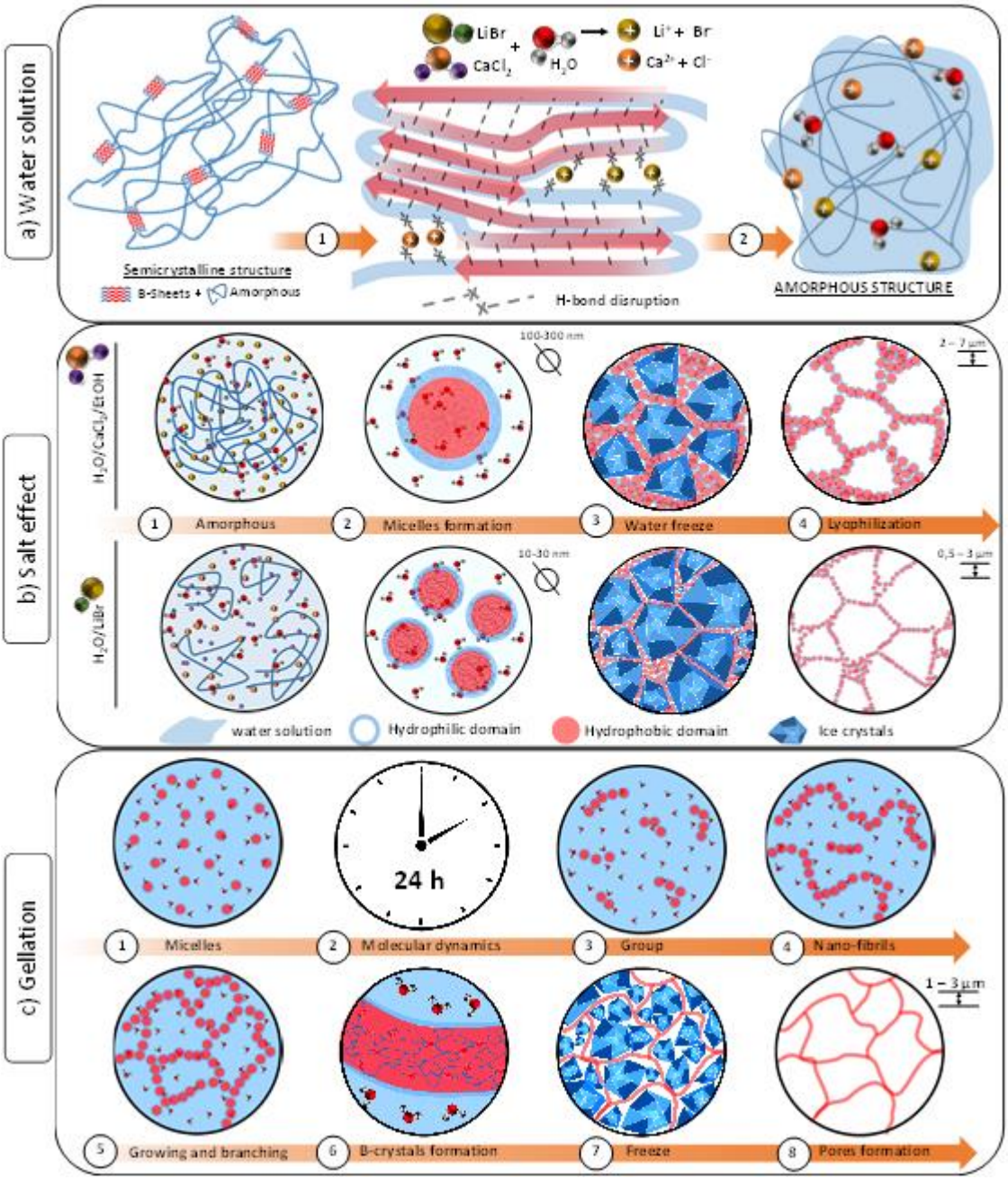

Figure 7 - Graphical representation of Silk Fibroin (SF) a) aqueous solution (β-sheets disruption), b) $CaCl_2$ and LiBr salts effect during solution and c) gelation process.

4.2. Processing effect on SF properties.

As it is shown in FTIR and XRD data, the secondary structure and crystallinity highly differ between samples. In Gel samples, the given longer molecular recombination time, promotes the formation of crystalline structures rich in β-sheets. These results also agree with the observed low intensity FTIR peaks at 2850 cm^{-1} in Gel samples (CaCl-Gel and LiBr-Gel), attributed to hydrogen bonding increase due to chains packing [28]. The

555 shorter time for molecular recombination of Lio samples, results in slightly ordered
556 structures with high RC amount (amorphous conformation). These data confirm the
557 strong effect of molecular recombination time for SF structure formation.
558 Foam samples present differentiated secondary structure and crystallinity (Figures 3 and
559 4), even though both samples have equally processed. As described by *D. Maniglio et al.*
560 [30] the SF foam is formed at the time that aqueous solution is extruded through the
561 nozzle. Also, foam was immediately freeze by liquid nitrogen bath. This leaves the SF
562 molecules without time for molecular recombination (Table 1). Thus, it can be suggested
563 that during foaming process, the higher micelles from $CaCl_2$ ternary solution, promote
564 more protein-protein interactions than LiBr solution. Consequently, in $CaCl_2$-Foam the
565 hydrophobic interactions are promoted and more crystalline domains are formed.
566 Processing methods induced molecular organization, as is described by TGA data, seems
567 to slightly affect samples thermal stability. However, a difference is observed between
568 solvents induced water retention, having the samples from $CaCl_2$ ternary solution greater
569 water amount (Figure 5a and 5b). Data suggest that bigger micelles formed in $CaCl_2$
570 ternary solution, retain a higher amount of water molecules inside, plasticising the
571 resulting samples.
572 DSC data shows a clear effect of processing on thermal transitions. As can be observed,
573 amorphous samples show the more pronounced transitions (both T_g and T_c), while
574 crystalline samples, practically lack them. Both T_g and T_c, are transitions related to free
575 domains mobility. Chains packing and consequent B structures presence, suppose the
576 formation of a cross-linked network in where the chains mobility is reduced by physical
577 nodes. As a consequence, greater B structures presence implies a minor mobility and
578 therefore, less pronounced thermal transitions.
579 No experimental evidence was found to relate the water uptake with the secondary
580 structure of SF. This suggests that the influence of microstructure prevails over the
581 secondary structure for water absorbance and retention, being the bean-like structure of
582 $CaCl_2$-Gel sample the configuration with major water retention ability.
583 The good stability of SF porous samples in water, confirm the potentiality of samples for
584 wet applications. $CaCl_2$-Lio sample is the only one not water stable, even when it has a
585 similar secondary conformation and crystalline organization than LiBr-Lio samples. The
586 main parameter which differs among both Lio samples is found on micelles formation
587 and the plasticisation level of the samples, being the $CaCl_2$-Lio the most plasticised one.

Data reveal once again the importance of the solvent contribution over samples properties and predict a water stability decrease with an increase on plasticisation.

Regarding to the effect of EtOH treatment, it is revealed a homogenous influence over almost all the parameters. It is known that EtOH highly interacts with water molecules, even more than SF (Figure 8a1). As consequence, during EtOH bath the H_2O molecules can link to EtOH. During the drying process and due to this interaction, bonded water and EtOH molecules are evaporated together, leaving the SF free of water. This SF dehydration, derives in more hydrophobic interactions, chains packing and crystalline domains increase (Figure 8a2) [32]. This effect, could be noted i) in SEM images where due to EtOH treatment, porous structures are contracted; ii) in FTIR and XRD, where the treated samples become highly crystalline Silk II (Figure 3 and 4); iii) in TGA where, thermal degradation was slightly delayed (Figure 5); iv) in DSC where highly stable and low mobile crystal domains lead to thermal transitions almost total loss (Figure 5) and v) in water behavior where all the structures gain water stability (Figure 6) .

The only characteristic not homogeneously influenced by EtOH treatment was the water uptake ability. This heterogeneity can be ascribed to the higher influence of the microstructure on water absorption. The observed water uptake decreasing with respect to EtOH untreated samples, (Supporting Figure 3a), is related to the structure contraction due to the dehydration (Figure 2g).

4.3. SF porous structures for water remediation.

Finally, SF adsorption ability for different heavy metal and metalloid ions, including As^{5+}, As^{3+}, Cr^{6+} and Cr^{3+} was studied. The selection of these ions is based on their varied chemistry and high toxicity in aqueous environments. In waters with pH 4, As^{5+} and Cr^{6+} are usually stabilized as negatively charged oxyanions like arsenate, chromate or dichromate [59]. On the contrary, $Cr^{3+}$is a hard cation that is stabilized as aquo-oxo species ($Cr(OH)^{2+}$ and Cr^{3+}) with neat positive charges [60]. Finally, As^{3+} is stabilized as neutral species. In general, the ions adsorption is driven by: i) electrostatic interaction with charged groups within the porous structure; ii) by anionic or cationic exchange processes where mobile ions within the SF structure could be replaced and iii) or direct interaction with reactive species. As adsorption data reveal (Figure S4), SF is affine to cationic species ($Cr(OH)^{2+}$ and Cr^{3+}), while practically does not show affinity for negative or neutral species. This behaviour suggests an electrostatic interaction between SF and cationic species ($Cr(OH)^{2+}$ and Cr^{3+}), mainly ascribed to the negative charge of SF

surface, result of isoelectric point differences between hydrophilic and terminal domains [16, 61, 62] (Figure 8a1). Additionally, it can be predicted that SF and $Cr(OH)^{2+}$ will form direct interactions between reactive –OH group of $Cr(OH)^{2+}$ and accessible amine groups of SF polypeptide chain, increasing the porous structures adsorption capacity [33, 63].

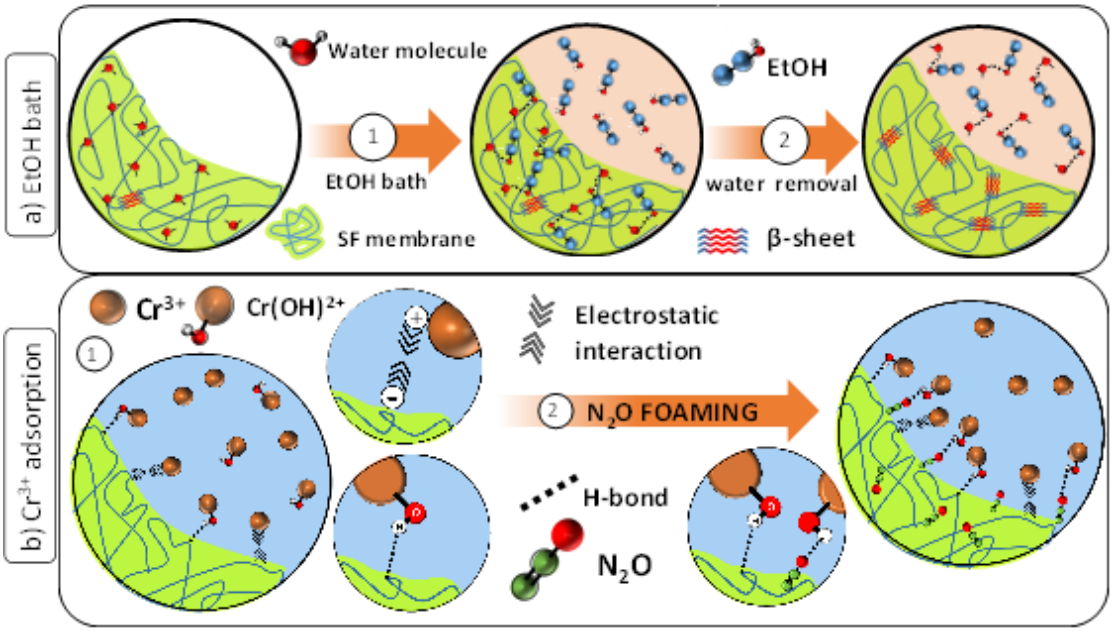

Figure 8. a) EtOH bath effect b) metals adsorption improvement by N_2O addition.

With respect to the effects of SF secondary structure and morphological characteristics in heavy metals adsorption, it can be stated that: i) Foam samples show larger adsorption values and ii) SF porous structures adsorption practically doubles after EtOH treatment. The higher adsorption ability of the Foam samples must be related to the processing conditions. During the foaming, SF is mixed with N_2O in order to generate pores by decompression. The gas molecules get trapped within the SF polypeptide chains forming interactions with chelate and hydroxyl groups [64] (Figure 8b2) [65]. Thus, it can be hypothesized that, these new SF-N_2O complexes may generate more accessible points in where $Cr(OH)^{2+}$ could link , increasing the SF adsorption capacity (Figure 8b2).

Regarding to Cr^{3+} adsorption after EtOH treatment, it seems that all the samples undergo an increase of their capacity. To explain this change, three considerations have been taking into consideration after EtOH treatment: i) all the samples do not reach a homogenous behavior, suggesting the effect of microstructure as additional factor; ii) the Cr^{3+} adsorption capacity increases despite of the decrease of samples water uptake (note

643 that $CaCl_2$-Gel sample in spite of having the major water uptake does not have the major
644 Cr^{3+} adsorption capacity) and; iii) SF negative charges did not increase during chains
645 packing, discarding the electrostatic interactions as the single reason for this effect [66].
646 Thus, we hypothesize that the dehydration caused by EtOH bath, generates new
647 accessible polar bonding points (where H_2O molecules were attached) in where more
648 $Cr(OH)^{2+}$ could be attached.
649 In this context, it can be concluded that, in SF porous structures, Cr^{3+} adsorption is mainly
650 driven by direct interactions. However, while H_2O molecules remain bonded to the
651 polypeptide structure (before EtOH treatment), the adsorption is driven by the
652 combination of electrostatic and direct interactions.
653 The obtained adsorption results can be compared with the ones from different natural
654 materials presented in Table 3. Actually, few works focusing on As and Cr absorption
655 can be found in the literature. As can be observed, most of the efforts have focused on the
656 use of chitosan, cellulose, plants or minerals. The present work demonstrates that SF is a
657 promising material, competitive with the aforementioned ones, to be used as adsorption
658 material for pollutants removal. In addition, the given routes for SF based porous
659 structures control, allowing also the possibility of developing composite materials, gives
660 the chance for further tailoring the structures for specific applications.
661
662 **Table 3.** Representative data of different natural materials used for heavy metals
663 adsorption.

Adsorbent	***Morphology***	***Pollutant / concentration* (mg/L)**	***Charge (g/L)***	***Adsorption (mg/g)***	***ref***
modified chitosan	crosslinked	Methylated Ar / 125	0.5	7.1 – 15.5	[67]
Cocoa shells	fibers	Cu / 45.5	40	2.6	[68]
Aluminosilicate geopolymer	powder	Pb, Ni, Hg Cu / 3000	5	200 - 600	[69]
wood	sawdust	Zn, Fe, Cu / 10	10	0.6 - 1	[70]
wool keratose /silk fibroin	Electrospinning mats	Cu^{2+} / 3.49	-	2.88	[17]
SF	Electrospinning mats	Cu^{2+} / 3.49	-	1.65	[17]
Malic acid/ chitosan	hydrogel beads	Cr(VI) / 100	1	383.2	[71]
waste cotton	cross-linked hydrogel	Pb / 7.6	1	7.5	[72]
This work	Porous	Cr^{3+} / 20	2	3.1	-

664

5. Conclusions

In order to expand the natural based materials applicability, the effect of different processing methods on Silk Fibroin (SF) porous structures properties has been addressed. For this purpose, six different SF structures with highly differentiated microstructure and porosity values above 94% where obtained from two dissolving agents, $CaCl_2$ and LiBr and three different regeneration procedures, including gelation, freezing and N_2O foaming.

It has been observed that $CaCl_2$/EtOH/H_2O ternary solution promotes SF molecules aggregation, increases the samples plasticization and induces the formation of wider leaf-like structures. On the contrary, LiBr aqueous solution favors the formation of thinner leaf-like structures with bigger interspersed pores.

SF gelation promotes molecular recombination, enables the polypeptide chains folding into highly crystallized structures and in combination with $CaCl_2$/EtOH/H_2O ternary solution, results in a bean-like microstructure. Directly lyophilized samples, contrary, promote amorphous structures and combined with LiBr solution, enable the formation of water soluble structures.

SF shows affinity for cationic species, which could be favored by N_2O gas foaming. EtOH treatment, leads to an increase of SF crystalline configuration that slightly slows down thermal degradation, increases samples water stability and promotes the ability for Cr^{3+} adsorption.

This demonstrated SF ability for heavy metals removal, as well as the capacity for controlling SF properties through processing, open a novel and promising investigation approach for the applicability of natural based materials and highlight SF porous materials aptitude for water remediation purposes.

Acknowledgements

The authors acknowledge the FCT (Fundação para a Ciência e Tecnologia) for financial support under the framework of Strategic Funding grants UID/FIS/04650/2020, and projects. PTDC/FIS-MAC/28157/2017 and PTDC/BTM-MAT/28237/2017. The authors also acknowledge the FCT for financial support under grant SFRH/ BPD/112547/2015 (C. M. C.). Financial support from the Spanish State Research Agency (AEI) and the

European Regional Development Fund (ERFD) through the project PID2019-106099RB-C43 / AEI / 10.13039/501100011033 and from the Basque Government Industry and Education Departments under the ELKARTEK, HAZITEK and PIBA (PIBA-2018-06) programs is also acknowledged.

References

1. Touchaleaume, F., et al., *Performance and environmental impact of biodegradable polymers as agricultural mulching films.* Chemosphere, 2016. **144**: p. 433-439.
2. Schou, P., *Polluting Non-Renewable Resources and Growth.* Environmental and Resource Economics, 2000. **16**(2): p. 211-227.
3. Blass, V., T.C. Chebach, and A. Ashkenazy, *Sustainable Non-Renewable Materials Management*, in *Sustainable Supply Chains: A Research-Based Textbook on Operations and Strategy*, Y. Bouchery, et al., Editors. 2017, Springer International Publishing: Cham. p. 87-118.
4. Chen, J.-S., C.K. Ober, and M.D. Poliks, *Characterization of thermally reworkable thermosets: materials for environmentally friendly processing and reuse.* Polymer, 2002. **43**(1): p. 131-139.
5. Mulinti, P., et al., *10 - Strategies to improve the hemocompatibility of biodegradable biomaterials*, in *Hemocompatibility of Biomaterials for Clinical Applications*, C.A. Siedlecki, Editor. 2018, Woodhead Publishing. p. 253-278.
6. Nguyen, T.P., et al., *Silk Fibroin-Based Biomaterials for Biomedical Applications: A Review.* Polymers, 2019. **11**(12): p. 1933.
7. Koh, L.-D., et al., *Structures, mechanical properties and applications of silk fibroin materials.* Progress in Polymer Science, 2015. **46**: p. 86-110.
8. Zhu, Z., T. Imada, and T. Asakura, *Preparation and characterization of regenerated fiber from the aqueous solution of Bombyx mori cocoon silk fibroin.* Materials Chemistry and Physics, 2009. **117**(2): p. 430-433.
9. Reizabal, A., et al., *Optimized silk fibroin piezoresistive nanocomposites for pressure sensing applications based on natural polymers.* Nanoscale Advances, 2019. **1**(6): p. 2284-2292.
10. Brito-Pereira, R., et al., *Silk fibroin-magnetic hybrid composite electrospun fibers for tissue engineering applications.* Composites Part B: Engineering, 2018. **141**: p. 70-75.
11. Reizabal, A., et al., *Tailoring silk fibroin separator membranes pore size for improving performance of lithium ion batteries.* Journal of Membrane Science, 2020. **598**: p. 117678.
12. Wang, Q., et al., *Facile production of natural silk nanofibers for electronic device applications.* Composites Science and Technology, 2020. **187**: p. 107950.
13. Zhu, B., et al., *Silk Fibroin for Flexible Electronic Devices.* Advanced Materials, 2016. **28**(22): p. 4250-4265.
14. Reizabal, A., et al., *Silk Fibroin Based Magnetic Nanocomposites for Actuator Applications.* Advanced Engineering Materials. **n/a**(n/a): p. 2000111.
15. Kapoor, S. and S.C. Kundu, *Silk protein-based hydrogels: Promising advanced materials for biomedical applications.* Acta Biomaterialia, 2016. **31**: p. 17-32.
16. Zhou, W., et al., *Removal of copper ions from aqueous solution by adsorption onto novel polyelectrolyte film-coated nanofibrous silk fibroin non-wovens.* Applied Surface Science, 2015. **345**: p. 169-174.
17. Ki, C.S., et al., *Nanofibrous membrane of wool keratose/silk fibroin blend for heavy metal ion adsorption.* Journal of Membrane Science, 2007. **302**(1): p. 20-26.

18. Gao, X., et al., *A silk fibroin based green nano-filter for air filtration.* RSC Advances, 2018. **8**(15): p. 8181-8189.
19. Xiao, S., et al., *Effective removal of dyes from aqueous solution using ultrafine silk fibroin powder.* Advanced Powder Technology, 2014. **25**(2): p. 574-581.
20. Drummy, L.F., et al., *Thermally Induced α-Helix to β-Sheet Transition in Regenerated Silk Fibers and Films.* Biomacromolecules, 2005. **6**(6): p. 3328-3333.
21. He, P., et al., *Complex micelles from the self-assembly of coil-rod-coil amphiphilic triblock copolymers in selective solvents.* Soft Matter, 2010. **6**(7): p. 1539-1546.
22. Kamalha, E., et al., *FTIR and WAXD Study of Regenerated Silk Fibroin.* Advanced Materials Research, 2013. **677**: p. 211-215.
23. Ming, J., F. Pan, and B. Zuo, *Influence factors analysis on the formation of silk I structure.* International Journal of Biological Macromolecules, 2015. **75**: p. 398-401.
24. Wilson, D., R. Valluzzi, and D. Kaplan, *Conformational Transitions in Model Silk Peptides.* Biophysical Journal, 2000. **78**(5): p. 2690-2701.
25. Lu, Q., et al., *Water-insoluble silk films with silk I structure.* Acta Biomaterialia, 2010. **6**(4): p. 1380-1387.
26. Cheng, Y., et al., *On the strength b-sheet crystallites of Bombyx mori silk fibroin.* Journal of The Royal Society Interface, 2014. **11**(96): p. 20140305.
27. Sashina, E.S., et al., *Structure and solubility of natural silk fibroin.* Russian Journal of Applied Chemistry, 2006. **79**(6): p. 869-876.
28. Kim, U.-J., et al., *Structure and Properties of Silk Hydrogels.* Biomacromolecules, 2004. **5**(3): p. 786-792.
29. Zhang, Q., S. Yan, and M. Li, *Silk Fibroin Based Porous Materials.* Materials, 2009. **2**(4): p. 2276-2295.
30. Maniglio, D., et al., *Silk fibroin porous scaffolds by N2O foaming.* Journal of Biomaterials Science, Polymer Edition, 2018. **29**(5): p. 491-506.
31. Chankow, S., S. Luemunkong, and S. Kanokpanont, *Conformational transitions of thai silk fibroin secondary structures*. 2016. 1-5.
32. Li, M., et al., *Controlling molecular conformation of regenerated wild silk fibroin by aqueous ethanol treatment.* Polymers for Advanced Technologies, 2003. **14**(10): p. 694-698.
33. G. Saiz, P., et al., *Chromium speciation in Zr-based Metal-Organic Frameworks for environmental remediation.* Chemistry – A European Journal. **n/a**(n/a).
34. Hoslett, J., et al., *Surface water filtration using granular media and membranes: A review.* Science of The Total Environment, 2018. **639**: p. 1268-1282.
35. Loh, Q.L. and C. Choong, *Three-Dimensional Scaffolds for Tissue Engineering Applications: Role of Porosity and Pore Size.* Tissue Engineering Part B: Reviews, 2013. **19**(6): p. 485-502.
36. Pizarro, J., et al., *Heavy metals in northern Chilean rivers: Spatial variation and temporal trends.* Journal of Hazardous Materials, 2010. **181**(1): p. 747-754.
37. Sereshti, H., M. Vasheghani Farahani, and M. Baghdadi, *Trace determination of chromium(VI) in environmental water samples using innovative thermally reduced graphene (TRG) modified SiO2 adsorbent for solid phase extraction and UV–vis spectrophotometry.* Talanta, 2016. **146**: p. 662-669.
38. Rai, D., B.M. Sass, and D.A. Moore, *Chromium(III) hydrolysis constants and solubility of chromium(III) hydroxide.* Inorganic Chemistry, 1987. **26**(3): p. 345-349.
39. Das, J. and P. Sarkar, *A new dipstick colorimetric sensor for detection of arsenate in drinking water.* Environmental Science: Water Research & Technology, 2016. **2**(4): p. 693-704.
40. Dhar, R.K., et al., *A rapid colorimetric method for measuring arsenic concentrations in groundwater.* Analytica Chimica Acta, 2004. **526**(2): p. 203-209.

41. Reizabal, A., et al., *Silk Fibroin Bending Actuators as an Approach Toward Natural Polymer Based Active Materials.* ACS Applied Materials & Interfaces, 2019. **11**(33): p. 30197-30206.
42. Hu, X., D. Kaplan, and P. Cebe, *Determining Beta-Sheet Crystallinity in Fibrous Proteins by Thermal Analysis and Infrared Spectroscopy.* Macromolecules, 2006. **39**(18): p. 6161-6170.
43. Zhang, H., et al., *Preparation and characterization of silk fibroin as a biomaterial with potential for drug delivery.* Journal of Translational Medicine, 2012. **10**(1): p. 117.
44. Sah, D.M. and K. Pramanik, *Preparation, characterization and in vitro study of biocompatible fibroin hydrogel.* AFRICAN JOURNAL OF BIOTECHNOLOGY, 2011. **10**: p. 7878-7892.
45. Fan, Z., et al., *Water-insoluble amorphous silk fibroin scaffolds from aqueous solutions.* Journal of Biomedical Materials Research Part B: Applied Biomaterials, 2020. **108**(3): p. 798-808.
46. Weska, R., et al., *Effect of Freezing Methods on the Properties of Lyophilized Porous Silk Fibroin Membranes.* Materials Research-ibero-american Journal of Materials - MATER RES-IBERO-AM J MATER, 2009. **12**.
47. Porter, D., et al., *A kinetic model for thermal degradation in polymers with specific application to proteins.* Polymer, 2009. **50**(7): p. 1814-1818.
48. Cebe, P., et al., *Fast Scanning Calorimetry of Silk Fibroin Protein: Sample Mass and Specific Heat Capacity Determination*, in *Fast Scanning Calorimetry*, C. Schick and V. Mathot, Editors. 2016, Springer International Publishing: Cham. p. 187-203.
49. Hu, X., D. Kaplan, and P. Cebe, *Effect of water on the thermal properties of silk fibroin.* Thermochimica Acta, 2007. **461**(1): p. 137-144.
50. Leghouchi, E., E. Laib, and M. Guerbet, *Evaluation of chromium contamination in water, sediment and vegetation caused by the tannery of Jijel (Algeria): a case study.* Environmental Monitoring and Assessment, 2008. **153**(1): p. 111.
51. Shen, T., et al., *Dissolution behavior of silk fibroin in a low concentration CaCl2-methanol solvent: From morphology to nanostructure.* International Journal of Biological Macromolecules, 2018. **113**: p. 458-463.
52. Kasoju, N., et al., *Silk fibroin gelation via non-solvent induced phase separation.* Biomaterials Science, 2016. **4**(3): p. 460-473.
53. Jin, H.-J. and D.L. Kaplan, *Mechanism of silk processing in insects and spiders.* Nature, 2003. **424**(6952): p. 1057-1061.
54. Cho, H.J., et al., *Molecular weight distribution and solution properties of silk fibroins with different dissolution conditions.* International Journal of Biological Macromolecules, 2012. **51**(3): p. 336-341.
55. Byette, F., et al., *Cell-culture compatible silk fibroin scaffolds concomitantly patterned by freezing conditions and salt concentration.* Polymer Bulletin, 2011. **67**(1): p. 159-175.
56. Chen, Z., et al., *Programing Performance of Silk Fibroin Materials by Controlled Nucleation.* Advanced Functional Materials, 2016. **26**(48): p. 8978-8990.
57. Um, I.C., et al., *The role of formic acid in solution stability and crystallization of silk protein polymer.* International Journal of Biological Macromolecules, 2003. **33**(4): p. 203-213.
58. Matsumoto, A., et al., *Mechanisms of Silk Fibroin Sol−Gel Transitions.* The Journal of Physical Chemistry B, 2006. **110**(43): p. 21630-21638.
59. Newcombe, G. and D. Dixon, *Interface Science in Drinking Water Treatment: Theory and Applications*. 2006: Elsevier Science.
60. Silva, B., et al., *The role of pH on Cr (VI) Reduction and Removal by Arthrobacter viscosus.* International Journal of Chemical and Biomolecular Engineering, 2009. **43**: p. 56.
61. Wang, X., et al., *Nanolayer biomaterial coatings of silk fibroin for controlled release.* Journal of Controlled Release, 2007. **121**(3): p. 190-199.

62. Dubey, P., et al., *Silk Fibroin-Sophorolipid Gelation: Deciphering the Underlying Mechanism.* Biomacromolecules, 2016. **17**(10): p. 3318-3327.
63. Aljeboree, A.M., A.N. Alshirifi, and A.F. Alkaim, *Kinetics and equilibrium study for the adsorption of textile dyes on coconut shell activated carbon.* Arabian Journal of Chemistry, 2017. **10**: p. S3381-S3393.
64. Cao, Q., et al., *Non-covalent interactions of nitrous oxide with aromatic compounds: Spectroscopic and computational evidence for the formation of 1:1 complexes.* The Journal of Chemical Physics, 2014. **140**(14): p. 144304.
65. Einarsdottir, O. and W. Caughey, *Interactions of the anesthetic nitrous oxide with bovine heart cytochrome c oxidase. Effects on protein structure, oxidase activity, and other properties.* Journal of Biological Chemistry, 1988. **263**(19): p. 9199-9205.
66. Lammel, A.S., et al., *Controlling silk fibroin particle features for drug delivery.* Biomaterials, 2010. **31**(16): p. 4583-4591.
67. Wei, Y.-T., Y.-M. Zheng, and J.P. Chen, *Uptake of methylated arsenic by a polymeric adsorbent: Process performance and adsorption chemistry.* Water Research, 2011. **45**(6): p. 2290-2296.
68. Meunier, N., J.-F. Blais, and R.D. Tyagi, *Selection of a natural sorbent to remove toxic metals from acidic leachate produced during soil decontamination.* Hydrometallurgy, 2002. **67**(1): p. 19-30.
69. Maleki, A., et al., *A green, porous and eco-friendly magnetic geopolymer adsorbent for heavy metals removal from aqueous solutions.* Journal of Cleaner Production, 2019. **215**: p. 1233-1245.
70. Balintova, M., S. Demcak, and B. Pagacova, *A study of sorption heavy metals by natural organic sorbents.* International Journal of Energy and Environment, 2016. **10**: p. 189-194.
71. Zhang, Y., et al., *Malic acid-enhanced chitosan hydrogel beads (mCHBs) for the removal of Cr(VI) and Cu(II) from aqueous solution.* Chemical Engineering Journal, 2018. **353**: p. 225-236.
72. Ma, J., et al., *Fast adsorption of heavy metal ions by waste cotton fabrics based double network hydrogel and influencing factors insight.* Journal of Hazardous Materials, 2018. **344**: p. 1034-1042.